Contents lists available at ScienceDirect

Journal of the European Ceramic Society

journal homepage: www.elsevier.com

Original Article

New spectroscopic and diffraction data to solve the vanadium-doped zircon pigment conundrum

Matteo Ardit[a,*], Giuseppe Cruciani[a], Francesco Di Benedetto[b], Lorenzo Sorace[c], Michele Dondi[d]

[a] University of Ferrara, Department of Physics and Earth Sciences, via Saragat 1, Ferrara, Italy
[b] University of Florence, Department of Earth Sciences, via La Pira 4, Florence, Italy
[c] University of Florence, Department of Chemistry 'Ugo Schiff', via della Lastruccia 3-13, Sesto Fiorentino, Italy
[d] CNR-ISTEC, Institute of Science and Technology for Ceramics, via Granarolo 64, Faenza, Italy

ARTICLE INFO

Keywords:
Colour
Crystal structure
EPR
Optical spectra
V^{4+}

ABSTRACT

The literature on V-doped zircon pigments offers a puzzling situation with unanswered questions about the origin of turquoise colour. In this study, new diffraction (XRPD) and spectroscopic (EPR, EAS) data were obtained on four industrial pigments, whose vanadium content is much higher than samples from previous investigations. Both EPR features and XRPD results indicate the occurrence of tetrahedrally-coordinated V^{4+} at the zircon interstitial site 16*g*. EPR spectra at 5 K exhibit a structured multiplet attributed to isolated V^{4+} ions and an exchange-narrowed line resulting by clustering of V^{4+} ions. The intensity of optical bands is stronger in samples affected by V^{4+} clusters. However, the turquoise colour stems from the window of transmitted green-bluish light, which depends on both the tail of the main optical band ($^2B \leftarrow {}^2A$) and the onset of charge transfer phenomena. Small variations in these two bands readily turn into a chromatic shift from light blue to green.

1. Introduction

The ceramic industry is currently utilizing only one pigment with colour between green and blue, namely in the turquoise-cyan range, that is vanadium-doped zirconium silicate [1,2]. Nickel-doped hibonite or Mn^{5+}-doped oxides were also proposed as turquoise pigment [3–5], but they never entered in the industrial use because of technological limits in ceramic processing.

Seabright [6] patented the V-doped zircon as ceramic pigment in 1948. Its peculiar turquoise colour soon attracted the academic interest and early attempts to explain the origin of colour go back to the 1960s [7–10]. Since the 1970s, the V-doped zircon has been a milestone of the "ceramic palette", being able to cover the wide colour space from light blue to green and, by mixing with Pr-doped zircon, to yellowish green [1,11]. However, the advent of inkjet printing, that since 2009 has almost completely replaced previous decoration techniques, changed drastically both technological requirements and colour demand for ceramic pigments [12].

On one side, inkjet printheads work properly only with submicronic pigments, a constraint which has imposed the colorant industry to a further process of micronization [13]. This makes conventional pigments more reactive (due to higher specific surface area), but it damages their crystal structure, leading eventually to amorphisation [14]. These drawbacks can be somewhat overcome by increasing the solid load of inks, but this has repercussions on ink viscosity and surface tension, which must be within the window acceptable by inkjet printers [15]. On the other side, digital decoration is managed by quadrichromy (four basic colours: Cyan, Magenta, Yellow and Black). This circumstance brought about a dramatic reduction of the potential candidates as pigments in digital inks [1,12]. In principle, V-zircon should be the best candidate for the Cyan ink, but strong limitations arise when the pigment is micronized then applied on glazes for ceramic tiles [13,14].

The ceramic pigment manufacturers faced the "digital era" by reformulating their recipes in order to get better performances. This improvement was successful for various pigments, including blue and black spinels, magenta malayaite, and particularly yellow zircon obtained by praseodymium doping [16–19]. Noteworthy the reason why V-doped zircon is unreliable for inkjet printing, while Pr-doped zircon is widely utilized, is not fully understood yet. A deeper comprehension

* Corresponding author.
Email address: harditster@gmail.com (M. Ardit)

https://doi.org/10.1016/j.jeurceramsoc.2018.07.033
Received 14 June 2018; Received in revised form 18 July 2018; Accepted 21 July 2018
Available online xxx
0955-2219/

of this different behaviour would pave the way to an actual engineering of micronized pigments, starting from a proper design of crystal structural features.

Vanadium may be in principle located at different sites of the zircon lattice, especially in the case of high V concentration, as in industrial pigments. The crystal structure of zircon ($ZrSiO_4$; s.g. $I4_1/amd$) consists of chains of alternating edge-sharing SiO_4 tetrahedra and ZrO_8 triangular dodecahedra running parallel to the *c*-axis. As shown in Fig. 1A, those chains are joined by edge-sharing ZrO_8 dodecahedra along the *ab*-plane, so that each ZrO_8 polyhedron shares edges with four adjacent ZrO_8 dodecahedra [20,21]. Both Zr^{4+} and Si^{4+} are located at crystallographic sites (Wyckoff positions 4*a* and 4*b*, respectively) with the same symmetry (i.e. -4*m*2 or D_{2d}), whereas O^{2-} finds place at the 16*h* position with site symmetry. *m*. or C_s. The polyhedral arrangement of the zircon structure gives rise to voids between tetrahedral and dodecahedral sites, i.e. potential interstitial sites within which impurity elements can be accommodated [21]. Among those interstitial sites, the tetrahedral site located at the 16*g* Wyckoff position (Fig. 1B) with symmetry 2 or C_2 has been proposed for hosting V^{4+} ions [22].

It is recognized how difficult is to keep under strict control all variables in the synthesis of V-doped zircon pigments [23–25]. Vanadium is more or less easily volatilized during calcination, that is usually carried out at temperatures between 800 and 1000 °C with various mineralizers, mostly alkaline fluorides [26–29]. Such mineralizers are necessary to get the formation of zircon, which takes place on zirconia by transportation of silicon and oxygen across the interface [8,23]. The role of fluorine is likely that of vehiculating silicon in the gaseous phase through SiF_4 complexes [26,27]. In the industrial practice, the starting batch contains the precursor (ammonium metavanadate) in excess with respect to the "optimal" doping, i.e. 3%–5% wt. as vanadium pentoxide, because some will be lost by volatilization [1,4]. Thus, pigment manufacturers cannot exactly predict the amount of vanadium actually inside the zircon structure, that is a consequence of synthesis conditions [23,27–29]. Although the vanadium concentration is the main factor controlling the intensity and stability of turquoise colour, other factors play a relevant role: amount and type of vanadium precursor, synthesis route, particle size, and so on [30–33].

In the literature, there is a long time debate about the valence, oxygen coordination, and localization of vanadium ions responsible of turquoise colour in the zircon crystal structure [8,22,34–47]. Although there is a large convergence on V^{4+} as the chromophore ion, opinions differ significantly about which site is hosting the V^{4+} ions in the zircon lattice. Such disparate viewpoints stem from a remarkably wide range of experimental techniques (Table 1) and produce a patchwork of useful observations, even though none of them individually conclusive. Interestingly, some papers relate the V^{4+} partition among the zircon sites to the amount of vanadium and/or the use of mineralizers [44,46,47]. It is worthwhile noting that most literature data refer to zircon doped with low to very low amount of vanadium, at variance with industrially manufactured pigments, which in most cases still rely on the original patent recipe [6].

The main goal of the present study is to shed light – by cross-checking literature data with new experimental results – on still unanswered questions about the valence state and location of vanadium ions inside the zircon lattice. This achievement would allow the full comprehension of colouring mechanisms in industrial pigments, with important repercussions on their technological properties and especially the behaviour during micronization and firing.

2. Materials and methods

Materials: four samples of V-doped zircon (named **BM61, TZ, 423** and **5108**, respectively) were investigated to include industrially manufactured turquoise pigments (supplied by four different colorant-makers) in order to widen the range of vanadium concentration and colour properties. No specific information is available on the industrial synthesis conditions and mineralizers employed, beyond a general description of the process [6].

2.1. Chemical and physical characterization

The chemical composition of industrial pigments was performed by X-ray Fluorescence Wavelength Dispersive Spectrometry (XRF-WDS) using a Panalytical Axios spectrometer with experimental conditions (power, voltage and current of the X-ray tube, diffracting crystal, detector window) tailored for each analyte. The sample was melted (1200 °C in platinum crucible with lithium borate-to-sample ratio 9:1) to get a glassy disc (50 mm diameter). Calibration of the counts x concentration straight lines were set up using zircon reference materials. The results obtained in this way (10 replicates) are reported in Table 2.

The morphology of pigment particles was observed under a Scanning Electron Microscope (SEM, Zeiss SUPRA 50VP). Pigment powders were scattered and glued on a copper support, then gold coated.

The particle size distribution was determined by X-ray monitoring of gravity sedimentation, using a Micromeritics SediGraph 5100 apparatus and applying the experimental conditions of ASTM C958 standard. Samples were dispersed by ultrasonic bath in a 0.5% W/W sodium hexametaphosphate aqueous solution. The median particle size (50th percentile of the cumulative curve) is reported in Table 2.

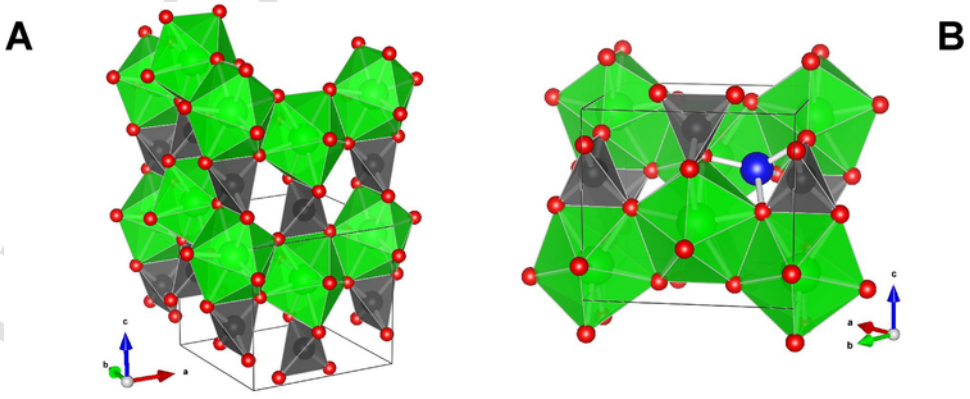

Fig. 1. Schematic representation of the $ZrSiO_4$ polyhedral arrangement in a perspective view along the *c*-axis where isolated SiO_4 tetrahedra share corners and edges with ZrO_8 dodecahedra. These latter are arranged in chains parallel to the *ab* plane through edge-sharing (A); polyhedral representation of the zircon tetragonal unit-cell (s.g. $I4_1/amd$) where Zr^{4+} (within dodecahedra) and Si^{4+} (within tetrahedra) occupy the 4*a* and 4*b* Wyckoff positions, respectively, whereas the 16*g* position is highlighted by means of a tetrahedrally coordinated atom within an interstitial void (B).

Table 1
Literature about localization in the zircon crystal structure of vanadium ions responsible of turquoise color. V(apfu): vanadium content in zircon (atoms per formula unit). V(prec): vanadium precursor. *miner*: use of mineralizers. Zr: cubic site 4*a*; Si: tetrahedral site 4*b*; Int: interstitial site 16*g*. Symbols indicate the probability level suggested by authors: conclusive or probable (++), possible (+), ruled out (no).

Paper	Ref.	Experimental techniques	V(apfu)	V(prec)	*miner*	Zr	Si	Int
Demiray et al. (1970)	[8]	XRD, EAS	N/A	NHV,V_2O_5	NaF	++		
Ball & Wanklyn (1976)	[10]	EPR, pEAS	N/A	V_2O_5	flux*	+	+	
Di Gregorio et al. (1982)	[34]	EPR, pEAS	~0.03	V_2O_5,NaV	flux		++	
Monrós et al. (1990)	[35]	XRD, EDS, FTIR	N/A	NHV	no	+		
Siggel & Jansen (1990)	[22]	XRD-SC	0-0.06	N/A	flux			++
Chandley et al. (1992)	[36]	AIC, EDS, XRD-SC	0.043	N/A	flux	+	+	no
Andrés et al. (1993)	[37] [38] [39]	AIC	*calc.*	*calc.*	no	+		
Beltrán et al. (1993)								
Beltrán et al. (1994)								
de Waal et al. (1996)	[40]	Raman	0.02-0.7	V_2O_5	no		++	
Ocaña et al. (1998)	[41]	XRPD, EXAFS-XANES, EPR	0.014- 0.043	V_2O_5	NaF	+	++	
Valentín et al. (1999)	[42]	XRD, EAS, EDS	0-0.03	V_2O_5	no		++	
Rubio-Puzzo et al. (2000)	[43]	PAC (Zr)	0.026	NHV	NaF	++	+	+
Torres et al. (2002)	[44]	XRPD	<0.05	V_2O_5	no		++	
			0.05-0.2	V_2O_5	no	++	+	
Niesert et al. (2002)	[45]	pEAS, QCC	0.76	V_2O_5	flux			++
Dajda et al. (2003)	[46]	NMR ^{29}Si, ^{91}Zr, ^{51}V, ^{17}O	<0.7	V_2O_5	NaF	++	++	
			>0.7	V_2O_5	NaF			+
Ardizzone et al. (2005)	[47]	XRPD, EPR, XANES, EAS	<0.05	VCl	no	++	++	
			>0.05	VCl	NaF			++

N/A: not available. AIC: ab initio calculations. EAS: Electronic Absorption Spectroscopy (p: polarized). EDS: Energy-Dispersive Spectroscopy. EPR: Electronic Paramagnetic Resonance. EXAFS: Extended X-ray Absorption Fine Structure. FTIR: Fourier-Transformed Infrared spectroscopy. NMR: Nuclear Magnetic Resonance. PAC: Perturbed Angular Correlations. QCC: Quantum Chemical Calculations. XANES: X-ray Absorption Near Edge Structure. XRD-SC: X-Ray Diffraction (Single Crystal). XRPD: X-Ray Powder Diffraction. *calc.* = calculated. Vanadium precursor: NHV = NH_4VO_3, NaV = $NaVO_3$, VCl, V_2O_5. Mineralizers: NaF or flux (lithium molybdate; *PbO or Bi_2O_3).

Table 2
Chemical composition, particle size distribution, and color of pigments and zircon crystal chemistry.

		Unit	**423**	**5108**	**BM61**	**TZ**	Exp. error
Pigment chemical composition	SiO_2	% wt	33.78	30.36	31.84	31.57	0.10
	TiO_2	% wt	0.06	0.10	0.08	0.12	0.01
	VO_2	% wt	2.62	3.13	3.15	2.76	0.02
	ZrO_2	% wt	60.66	62.50	61.81	61.74	0.20
	HfO_2	% wt	1.14	1.22	1.17	1.20	0.02
	Al_2O_3	% wt	1.37	0.67	0.62	0.35	0.02
	Fe_2O_3	% wt	0.08	0.12	0.11	0.09	0.01
	Na_2O	% wt	0.90	0.66	0.09	1.50	0.02
	P_2O_5	% wt	0.33	0.28	0.33	0.15	0.02
Zircon crystal chemistry	SiO_2	% mol	42.86	50.13	43.89	42.34	0.20
	ZrO_2	% mol	53.04	45.58	51.29	52.55	0.20
	HfO_2	% mol	0.58	0.52	0.57	0.60	0.02
	VO_2	% mol	3.52	3.77	4.25	4.50	0.02
occupancy site 4a (Zr + Hf)		apfu	1.072	0.922	1.037	1.063	0.005
occupancy site 4b (Si)		apfu	0.857	1.003	0.878	0.847	0.005
occupancy site 16g (V)		apfu	0.070	0.075	0.085	0.090	0.001
median particle size		μm	6.2	4.0	5.0	5.2	<0.1
Pigment color	L* (brightness)	%	70.5	72.9	69.7	67.7	0.3
	a* (green coordinate)	%	−11.6	−10.8	−10.7	−12.3	0.1
	b* (blue coordinate)	%	−20.4	−8.6	−13.7	−14.3	0.1
	*C (chroma)	%	23.4	13.8	17.4	18.8	0.2
Optical density (640 nm)		K/S	2.0	1.7	3.1	2.6	<0.1

The colour was measured on pigment powders by Hunterlab Miniscan MSXP4000 spectrophotometer equipped with an integrating sphere (illuminant D65, detection angle 8°, 5 replicates). The results are expressed in CIE L*a*b* coordinates, where L* is brightness (100 = white, 0 = black) while a* and b* are chromatic coordinates (+a* = red, –a* = green, +b* = yellow, –b* = blue) and C* = $(a^{*2} + b^{*2})^{0.5}$. Averaged values can be found in Table 2.

2.2. X-ray diffraction data collection and Rietveld refinements

X-ray powder diffraction measurements were performed at room temperature using a Bruker D8 Advance diffractometer on a Bragg-Brentano geometry with a X-ray tube operating at 40 kV and 40 mA. Experimental data were collected by means of a Si(Li) solid-state detector set to discriminate Cu $K\alpha_{1,2}$ radiation in the 5–130° 2θ angular range, with a counting time of 10 s per 0.02° 2θ step.

Structural parameters were determined from whole pattern profile fitting of the diffraction data by the Rietveld method using the GSAS code implemented into the EXPGUI interface [48,49]. The presence of associated phases, detected in variable amounts as reported in Table 3, was accounted for by carrying out multiphase refinements in which only the scale factors and the cell parameters were varied, except for the zircon main phase. The starting structural models employed during the Rietveld refinement were those of Kolesov et al. [50] for the zircon structure (tetragonal s.g. $I4_1/amd$), Hill et al. [51] for the baddeleyite structure (monoclinic s.g. $P2_1/c$), and Baur et al. [52] for the low quartz structure (trigonal s.g. $P3_121$). Peak profiles were modeled by a pseudo-Voigt function, with the peak cut-off set to 0.05% of the peak maximum, by means of three Gaussian terms (i.e., GU, GV, and GW, respectively), and the two Lorentzian broadening coefficients (i.e., LX, and LY, respectively) plus an asymmetry contribution. Besides 18 shifted Chebyshev polynomial coefficients to reproduce the background and a scale factor, the refinements included cell parameters (*a*- and *c*-axis), oxygen atomic coordinates (*y* and *z*), and isotropic atomic displacement parameters (U_{iso}) of the zircon phase.

2.2.1. Refinement strategy and evidence of V^{4+} location

Several refinement strategies were explored. Specifically, structural models with a full replacement of V^{4+} (in its stoichiometric amount) for both Zr^{4+} and Si^{4+} at the 4*a* cubic and 4*b* tetrahedral cationic sites, respectively, as well as refinement with partial substitutions of V^{4+} for Si^{4+} at the 4*b* site coupled with a small amount of V^{4+} at the 16*g* interstitial site were employed. Due to the "constrained" zircon structure (where only *a* and *c* unit-cell parameters, *y* and *z* oxygen atomic coordinates, and isotropic atomic displacement parameters (U_{iso}) can be refined), those previous attempts didn't lead to an unambiguous structural model (i.e., very few differences among the reliability indexes were observed).

The main evidence of the possible location of vanadium cations was derived from residuals of electron density calculated by mean of delta Fourier maps. Indeed, for all the investigated samples some electron density residuals (ranging from 0.30 to 0.45 e^- Å^{-3}) at the 16*g* interstitial site were detected. Fig. 2A highlights some electron density residuals around Zr and Si cations, and the location of well defined electron density residuals at the 16*g* interstitial position the latter being consistent with local occurrence of V ions within a few unit cells averaged by symmetry constraints all over the crystal structure.

Agreement factors and refinement details are listed in Table 3. Unit-cell parameters, vanadium content, selected metal–oxygen bond distances, bond angles, and polyhedral volumes of the zircon structure for the investigated samples are summarized in Tables 3 and 4. The Rietveld plot for the sample **TZ** is reported in Fig. 2.

2.3. Electronic Absorption Spectroscopy

Optical measurements were performed by Electronic Absorption Spectroscopy (EAS) in diffuse reflectance (Perkin Elmer λ19 spectrophotometer, 300–2500 nm range, 0.1 nm step size, $BaSO_4$ integrating sphere, white reference material: $BaSO_4$ pellet). Reflectance (R_∞) was converted to absorbance (K/S) by the Kubelka-Munk equation: $K/S = (1-R_\infty)^2 \cdot (2R_\infty)^{-1}$ [53]. Each one of the three absorbance bands in the NIR-visible-UV range was fitted with a Gaussian function (PFM, OriginLab) initially centred on peak maxima and going to convergence by an automatic procedure. By this way, band energy (centroid) and width (Full Width at Half Maximum, FWHM) were obtained, which experimental error, including background correction and reproducibility, is around 2%.

2.4. Electron Paramagnetic Resonance

X-band (ν ca. 9.4 GHz) Electronic Paramagnetic Resonance (EPR) spectra were measured on powder samples using a Bruker Elexsys E500 spectrometer (Bruker GmbH) equipped with a with a SHQ cavity and a ESR900 continuous flow ^{4}He cryostat (Oxford Instruments). Spectra were registered at different temperatures in the range 5–298 K.

3. Results and discussion

3.1. General features

Ceramic pigments are manufactured by industry with a rather narrow particle size distribution achieved by jet milling. In the case of zir-

Table 3
Quantitative phase analysis, goodness of fit (agreement factors), and refinement details of analyzed samples from X-ray powder diffraction. Furthermore, agreement factors, vanadium content, and unit-cell parameters for the zircon structure. Standard deviations are within parentheses.

Sample	**423**	**5108**	**BM61**	**TZ**
Quantitative phase analysis (wt %)				
zircon ($ZrSiO_4$)	86.3(3)	93.9(1)	86.8(3)	87.6(3)
baddeleyite (ZrO_2)	2.7(5)	6.1(6)	5.1(6)	3.6(6)
low quartz (α-SiO_2)	11.0(9)	–	8.2(9)	8.8(9)
Agreement factors and refinement details				
R_{wp}	0.0974	0.0915	0.1007	0.0989
R_p	0.0712	0.0676	0.0755	0.0718
No. of data	6250	6250	6250	6250
No. of variables	49	43	49	49
$R(F^2)$	0.0484	0.0340	0.0351	0.0347
$ZrSiO_4$ (s.g. $I4_1/amd$)				
No. of reflections	138	138	139	139
$R(F)$	0.0232	0.0164	0.0171	0.0167
Vanadium content, xV^{4+} (apfu):				
	0.071	0.075	0.084	0.090
Unit-cell parameters				
$a = b$ (Å)	6.61183(4)	6.61344(7)	6.61529(7)	6.61562(7)
c (Å)	5.99409(4)	5.99620(7)	6.00212(8)	6.00189(8)
V (Å^3)	262.040(4)	262.259(7)	262.665(7)	262.681(8)

Notes: data on the vanadium content have been obtained by weighting the VO_2 content from the chemical XRF analysis for the amount of the associated phases.

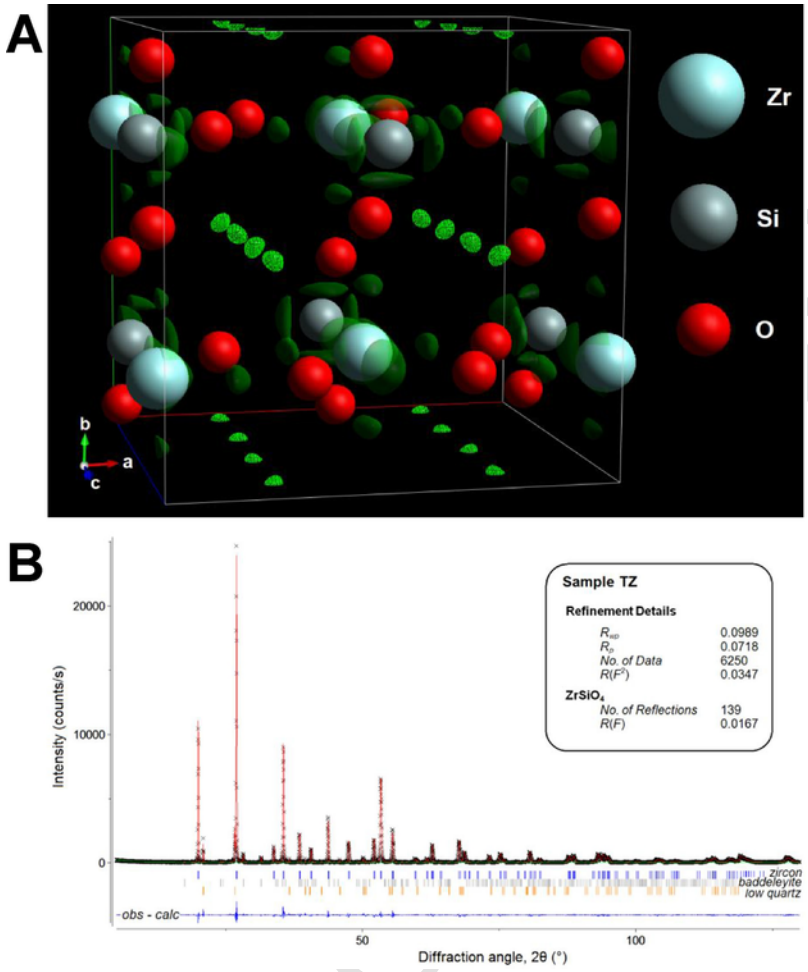

Fig. 2. 3-dimensional perspective of the ZrSiO4 unit-cell (sample **TZ**) with highlighted electron density residuals around Zr and Si cations, and the location of well defined electron density residuals at the 16*g* interstitial site (A); and, final Rietveld fit for the sample **TZ** (B). The experimentally observed data are indicated by crosses, the calculated pattern is the continuous line among crosses, and the lower curve is the weighted difference between calculated and observed patterns (obs-calc). Vertical ticks mark the position of allowed reflections for the crystalline phases present in the sample (i.e., zircon, baddeleyite, and low quartz, respectively).

Table 4
Final atomic coordinates, atomic displacement parameters (U_{iso} in Å^2 × 100), selected interatomic bond distances (Å), bond angles (°), and polyhedral volumes (Å^3) for $ZrSiO_4$ structures. Values within parentheses represent estimated standard deviations.

Sample		**423**	**5108**	**BM61**	**TZ**
Atomic coordinates* and ADPs					
Zr^{4+}	U_{iso}	0.23(2)	0.31(2)	0.27(2)	0.30(2)
Si^{4+}	U_{iso}	0.25(4)	0.19(4)	0.15(4)	0.12(4)
O^{2-}	*y*	0.0692(1)	0.0691(1)	0.0679(1)	0.0691(1)
	z	0.1926(1)	0.1932(1)	0.1944(1)	0.1934(1)
	U_{iso}	0.78(6)	1.01(5)	0.95(6)	0.99(6)
Interatomic bond distances					
	Zr—O'(x4)	2.149(1)	2.149(1)	2.144(1)	2.151(1)
	Zr—O''(x4)	2.248(1)	2.252(1)	2.264(1)	2.255(1)
	Si—O(x4)	1.620(2)	1.619(2)	1.621(2)	1.619(2)
	Zr—Si	2.997(1)	2.998(1)	3.001(1)	3.001(1)
Bond angles					
	Zr—O—Zr	111.26(3)	111.13(3)	110.95(3)	111.05(3)
	Zr—O—Si	100.33(4)	100.24(3)	99.85(4)	110.26(4)
	Zr—O—Si	148.41(4)	148.63(4)	149.20(5)	148.68(5)
Polyhedral volumes					
	ZrO_8	19.073	19.127	19.185	19.175
	SiO_4	2.083	2.081	2.098	2.082

Notes: Both Zr^{4+} and Si^{4+} atoms at special positions: Zr coordinates: $x = 0$, $y = ¾$, and $z = ⅛$; Si coordinates: $x = 0$, $y = ¾$, and $z = ⅝$. The *x* coordinate for the O^{2-} atom is equal to 0.

con pigments, this distribution range is comprised between 1 and 20 μm (98%) with 80% of the population from 3 to 10 μm approximately (Fig. 3A). The median particle size is in the order of 4–6 μm (Table 2). Jet milling allows maintaining in many cases the crystal shape of as-synthesized zircon particles, as it can be appreciated from SEM micrographs (Fig. 3B).

The chemical composition of pigments is characterized, along with the major constituents of zircon (ZrO_2 and SiO_2), by significant amounts of the chromophore (VO_2) and HfO_2 (since Hf^{4+} is a natural vicariant of Zr^{4+}). The minor content of Na_2O is a remnant of mineralizers, while the small amounts of Al_2O_3, Fe_2O_3, TiO_2 and P_2O_5 presumably stem from post-calcination contamination (during removal from refractory crucibles or milling) and/or impurities of precursors (Table 2). As a consequence, only Zr, Hf, Si and V enter the zircon structure, the other analytes being likely present as secondary phases. The composition of zircon was recalculated on this assumption, by subtracting the contribution of other crystalline phases, resulting in the crystal chemistry shown in Table 2. By this way, Zr (+Hf) occupancy of the cubic site is clearly higher than Si occupancy of the tetrahedral site, instead of the expected 1:1 ratio. Exception is the only sample (**5108**) without quartz, but with some zirconia excess, that is odd and let envisage the occurrence of amorphous silica, easy to form in some synthesis conditions [55]. Therefore, the Zr/Si ratio >1 is compatible with a preferential localization of vanadium at a tetrahedral site, but not at the cubic site. The occurrence of fluorine (not detectable by XRF) into the zircon structure was reported in the literature for both pigments and crystals obtained by hydrothermal synthesis in F-rich environment. In particular, fluorine is supposed to substitute oxygen [27,28] or replace silicon as tetrahedral nests $F_n(OH)_{4-n}$ [56,57]. In both cases, the incorporation of fluorine into the zircon structure led to a contraction of the unit cell volume. In our samples, a conspicuous expansion of the unit cell volume is observed – as it will be discussed in Section 3.3.1 – thus, any significant incorporation of fluorine can be ruled out.

The industrial pigments exhibit a different turquoise colour (Table 2). A significant variance is found for the blue component ($-8.6 < b^* < -20.4$) while the green component fluctuates in a rather narrow range ($-10.7 < b^* < -12.3$). These differences translate into a more or less intense turquoise shade ($13.8 < C^* < 23.4$) in decreasing order: **423** > **TZ** > **BM61** > **5108**. Interestingly, the chroma values scale linearly with the median particle size: the finer the dimension of individual pigment grains, the lower the C* values. However, this trend does not hold with the optical density (i.e., the intensity of the main optical band in Fig. 3A) implying a not trivial relationship between the optical spectrum and colour rendering that will be discussed in detail in Section 4.

3.2. Phase composition

As reported in Table 3, the tetragonal zircon structure (s.g. $I4_1/amd$) is the major phase in all samples. The amount of $ZrSiO_4$ ranges from a minimum of 86% (sample **423**) to a maximum of 94% (sample **5108**). Therefore, as typical in the industrial production, the analyzed samples are not strictly monophasic. The variable amount of associated phases, i.e., low quartz ($0 < SiO_2 < 11\%$) and baddeleyite ($3 < ZrO_2 < 6\%$), refers to unreacted precursors related to a slow reaction kinetics and/or low temperatures of calcination, which led to an incomplete crystallization of the zircon structure. The occurrence of a glassy phase, accounting for the impurities of Na, Al, P and Fe, is possible, but surely limited to 1% by weight or so (thus, resulting below the detection limit by XRPD).

As a matter of fact, the presence of associated phases could complicate the effective vanadium incorporation into the $ZrSiO_4$ lattice. A hypothetical incorporation of V^{4+} into the ZrO_2 lattice would provoke a volumetric shrinkage (since the ionic radii of heptacoordinated Zr^{4+} and V^{4+} are 0.78 and 0.65 Å, respectively); on the contrary, the lattice of SiO_2 would undergo a significant increase (i.e., the ionic radius of tetracoordinated Si^{4+} is 0.26 Å [58], whereas that estimated for $^{[IV]}V^{4+}$ is 0.46 Å). On the other hand, the unit-cell volumes of quartz and baddeleyite have a negligible variation, i.e. about 0.1% on average, with respect to pristine phases. Therefore, a significant vanadium incorporation into the lattice of ZrO_2 and/or SiO_2 can be excluded. Furthermore, as discussed in depth in the next section, the incorporation of V^{4+} in the $ZrSiO_4$ main phase is confirmed by large variations on the unit-cell volume and lattice parameters.

3.3. Crystal structure

3.3.1. Unit-cell volume and lattice parameters

Lattice parameters (axes *a* and *c*) and unit-cell volume (*V*) for the investigated zircon structures are reported in Table 3. In order to visualize their evolution and highlight possible anisotropies, the obtained data are compared with those of literature [22,32,36,41,42] as a function of the vanadium content (x_V^{4+}) in Fig. 4.

The incorporation of vanadium into the zircon lattice is clearly testified by a progressive and remarkable increase of both unit-cell volume (Fig. 5A) as well as *a* and *c* lattice parameters (Fig. 4B and C) with the vanadium concentration. In particular, a volumetric deviation $\delta V = 2.2$ Å^3 is observed between the undoped sample of Torres et al. [32] and the sample **TZ** (i.e. the one with the highest vanadium content). The occurrence of such structural expansion coupled with information on the phase composition (see previous paragraph) strongly suggests that the V^{4+} should substitute for a smaller ion (i.e. an isova-

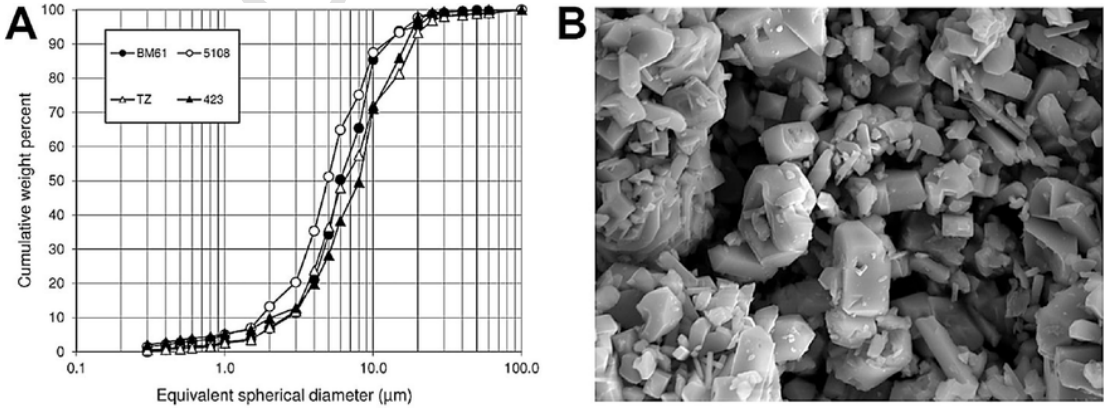

Fig. 3. Particle size distribution of pigments (A) and SEM micrograph (field 35 × 26 μm) of pigment **TZ** (B).

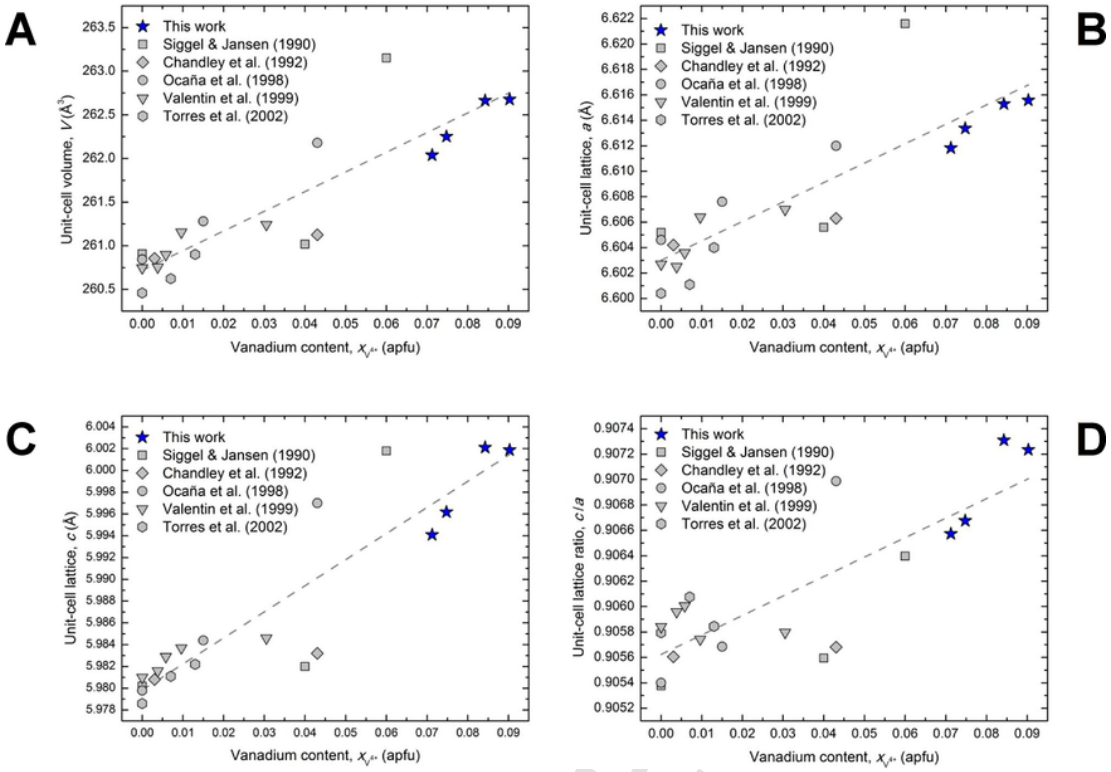

Fig. 4. Variation of the unit-cell volume (A), *a* and *c* lattice parameters (B and C), and *c*/*a* ratio (D) as a function of the vanadium content (x_V^{4+}). Error bars are within the symbol size. Dashed lines are a reader's eye guide.

lent substitution with Si^{4+} at the tetrahedral site 4*b*) or should be hosted at an interstitial site (e.g. at the tetrahedral site 16*g*), the lattice electroneutrality being maintained by Si vacancy. Furthermore, the lattice response to the vanadium incorporation is anisotropic. Fig. 5D shows that the *c* lattice parameter expands more rapidly than *a* with the V^{4+} content, meaning that a preferential expansion occurs along the chains of alternating edge-sharing SiO_4 and ZrO_8 polyhedra.

3.3.2. V-doped zircon structural features

In order to get further insights on the possible location of vanadium ions within the zircon structure, we report here a systematic description of the structural changes by means of the cation-anion interactions for atoms centred at sites with Wyckoff position 4*a*, 4*b*, and 16*g*, respectively. Fig. 5 shows the variation of the mean metal-oxygen bond distances at the cubic (A), tetrahedral (B), and interstitial sites (C) for samples from literature [22,32,36] and those investigated in this work as function of their nominal vanadium content.

Although slightly scattered, data plotted in Fig. 6 define three clearly distinct patterns. The effect of the vanadium incorporation into the zircon lattice leads to an opposite response of the mean bond distances of the cations centred at the cubic and tetrahedral sites. Specifically, while the mean ⟨Zr–O⟩ distances (site 4*a*) undergo a bond lengthening (Fig. 5A), the mean ⟨Si–O⟩ distances (site 4*b*) are subjected to a bond length decrease (Fig. 5B). A vanadium substitution occurring at the 4*a* site or at the 4*b* site should be nevertheless characterized by an opposite slope with respect to what observed. Indeed, in terms of ionic radii, the isoelectronic substitutions $^{[VIII]}Zr^{4+}$ (i.r. 0.84 Å) ↔ $^{[VIII]}V^{4+}$ (i.r. 0.72 Å) and $^{[IV]}Si^{4+}$ (i.r. 0.26 Å) ↔ $^{[IV]}V^{4+}$ (i.r. 0.46 Å) should provide a bond shortening/lengthening at the 4*a*/4*b* site, respectively.

The last trend, i.e., the increase of the bond distances at the site 16*g* as a function of the vanadium content (Fig. 6C), is consistent with the incorporation of V^{4+} ions at the interstitial site. This last evidence is also in good agreement with the V—O bond distances provided by Ocaña et al. [41] from XAS measurements.

3.4. Optical properties

Optical spectra exhibit light absorptions in four distinct ranges in the NIR, visible and UV (Fig. 6).

The optical bands in the NIR (~7000 cm^{-1}) and in the visible spectrum (at ~15,600 cm^{-1} with a shoulder at ~12,300 cm^{-1}) is completely different from optical patterns of V^{3+} and V^{5+} [59,60] and are attributable to crystal field transitions of V^{4+}. The optical spectrum of vanadium doped zircon is also clearly distinct (Fig. 7A) from those of vanadyl ion in cavansite [61,62] and apophyllite [63,64]. Similarities may be seen with spectra of V^{4+} in tetrahedral coordination at the SiO_4 site in Mg_2SiO_4 or at the GeO_4 site in Ca_2GeO_4 [65] even though with conspicuous differences in the band energies (Fig. 7A). The broad absorption extended over the UV range is likely to be a jumble of metal-oxygen charge transfers and further colour centres (induced by lattice defects, for instance caused by comminution).

Strict analogies exist in the V^{4+} optical fingerprint of compounds isostructural with zircon, i.e. coffinite and its germanate correspondent [34], besides the lower energy of electronic transition in Th phases (Fig. 7B). The features of the three optical bands in the NIR and visible ranges are summarized in Table 5. They can be attributed, with reference to the energy levels diagram of Fig. 3, to electronic transitions of V^{4+} in tetrahedral coordination at the interstitial site with C_2 symmetry (Fig. 7C). The resulting energy and width values of bands are very close in all pigments under examination, as their relative intensity, once normalized to the maximum absorbance of the main peak (Table 5).

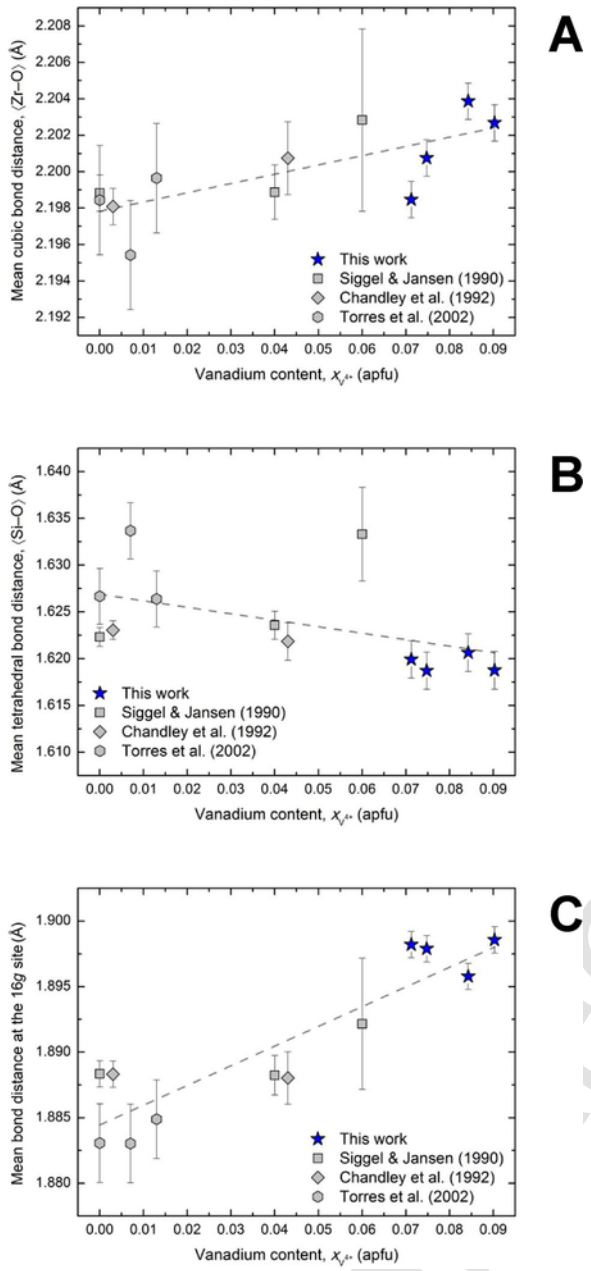

Fig. 5. Variation of the mean metal-oxygen bond distances at the cubic 4*a* (A), the tetrahedral 4*b* (B), and interstitial 16*g* (C) sites as a function of the vanadium content (x_V^{4+}). Dashed lines are reader's eye guides.

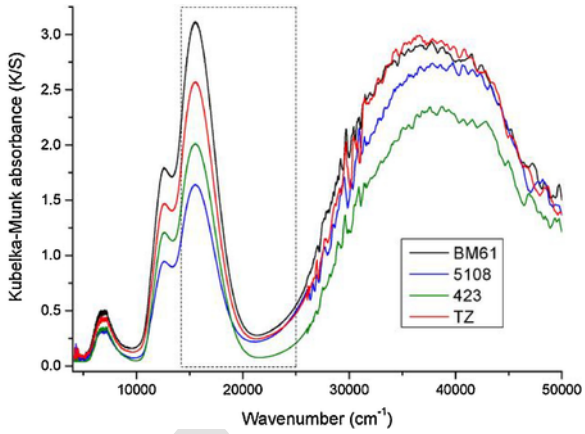

Fig. 6. EAS spectra of the four zircon pigments investigated in this study. The dotted window evidences the visible range.

3.5. Electron Paramagnetic Resonance

The room temperature EPR spectra of the different samples reveal the presence of numerous paramagnetic signals. From the intensity-to-noise ratio, all registered signals are attributed to species occurring as impurities in the sample (Table 2). Among them, the presence of Fe^{3+}, both in concentrated and diluted magnetic environment, and the absence of signals clearly due to V^{4+} or VO^{2+}, have to be highlighted.

The EPR spectra, registered as a function of the temperature in the range between 298 and 5 K, of two representative samples, **423** and **5108**, are shown in the Fig. 8A and B, respectively.

The two sets of spectra present a common evidence, i.e. the appearance at $T < 220$ K of a strong Lorentzian line at B values of ~350 mT, the intensity of which increases with decreasing temperature. Conversely, its width markedly decreases. The spectra registered at 5 K on both samples reveal the presence of a structured EPR signal, attributed, on the basis of its average resonant field (centred at ~343.9 mT, corresponding to a g value of 1.954), and on the appearance of an hyperfine structure, to V^{4+} a single V^{4+} species (Fig. 9).

The spectrum of Fig. 9 also reveals an apparent anisotropy of the Zeeman and hyperfine interactions. Both interactions were parameterised through the use of numerical simulations, performed by using Easyspin [66]. The best fit results are listed in Table 6. The numerical simulation was carried out under the assumption of an axial anisotropy, because the small splitting induced by a further decrease in the symmetry of the V^{4+}, as that expected for e.g. the 16*g* site, would have been hindered by the relatively large line width, ΔB. A definitely better agreement is obtained including in the fit an unstructured Lorentzian line centred at the same magnetic field value, the width of which is ~47.5 mT. These are clear features of a V^{4+} exchange narrowed line, as already observed for Mn(II) in ZnS sphalerite [67], and thus can be attributed to clusters of V^{4+} ions sitting closely to each other.

These two signals, i.e. the single narrow line appearing at $T < 220$ K and the V^{4+} spectrum occurring at 5 K, are consistent with previous results in the literature, many authors having identified either one or the other, or both [10,34,41,45,47]. Some authors have pointed out EPR features different from those observed here: e.g. Ardizzone et al. [47] have described a completely different set of results, where room temperature V^{4+} signals are occurring in blue zircon samples. A scheme of the results obtained in the literature, together with the relative attribution, is proposed in Table 7.

In the literature, the structured low-*T* multiplet and the narrow line have been attributed to different species of V in the sample: the former to V^{4+} as isolated ion (attributed either to the dodecahedral, or to the tetrahedral D_{2d} site, the signal of which disappears at $T > 20$ K due to the presence of a vibronic coupling [34]), and the latter to clusters of V^{4+} (closely localised in the zircon structure). The present data confirm both attributions. Namely, the multiplet observed at 5 K is characterized by a set of Hamiltonian parameters in good agreement with those previously reported [10,34,41,45]. A point in favour to the attribution of the narrow line to clusters of V^{4+} relies in the fact that the V^{4+} hyperfine multiplet can be observed also in samples not showing the narrow line at $20 < T < 220$ K. The contingent presence and the variable relevance of the narrow line is thus linked to the features of the synthesis.

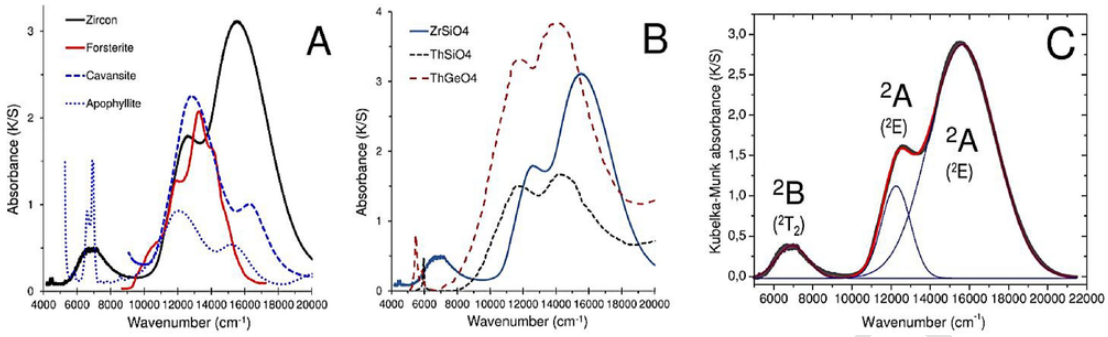

Fig. 7. Optical spectra of vanadium-bearing phases: (A) zircon versus minerals containing four- or five-coordinated V^{4+} or vanadyl ion VO^{2+} [61,62,65]; (B) zircon versus isostructural thorium silicate and germanate [34]; (C) attribution of optical bands in zircon pigments to electronic transitions of V^{4+} in the coordination at the site 16*g*. Parent tetrahedral symmetries are reported in brackets.

Table 5
Optical properties of V-doped zircon (industrial pigments) in comparison with literature data.

Electronic transition	Optical band features	**423**	**5108**	**BM61**	**TZ**	$ZrSiO_4$ [34]
^2A (^2E)	energy (cm^{-1})	15640	15630	15640	15630	15720
	energy (normalized)	1.00	1.00	1.00	1.00	1.00
	FWHM (cm^{-1})	4080	3930	4010	3960	–
^2A (^2E)	energy (cm^{-1})	12,300	12280	12250	12270	12500
	energy (normalized)	0.41	0.41	0.39	0.39	0.40
	FWHM (cm^{-1})	1640	1690	1730	1700	–
^2B ($^2T_2$)	energy (cm^{-1})	7010	6950	6940	6950	7040
	energy (normalized)	0.16	0.19	0.14	0.15	0.25
	FWHM (cm^{-1})	1800	1960	1850	1840	–

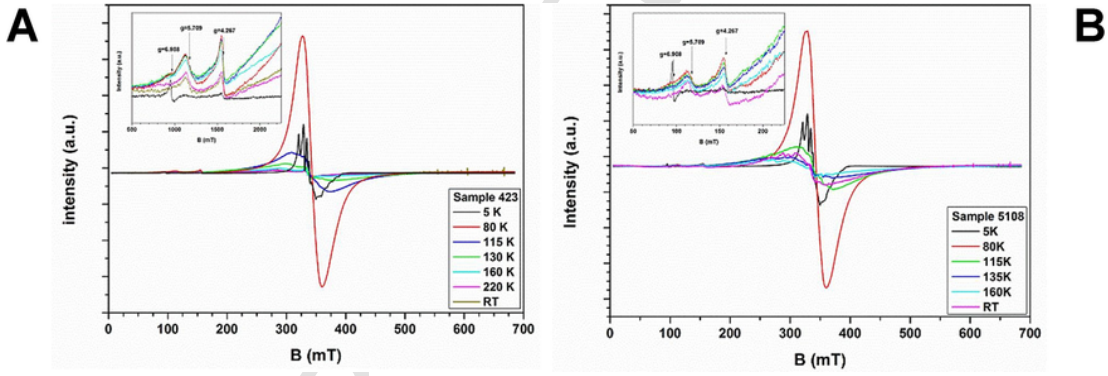

Fig. 8. EPR spectra of the **423** (A) and **5108** (B) samples, recorded at different temperatures in the range 5–298 K. All spectra were registered using the same attenuation value (15 dB), with the exception of those at 5 K that were registered at 55 dB attenuation. In the insets, a zoom of the paramagnetic signals at low magnetic field values is provided.

4. Discussion

The whole set of the present data, while confirming most of the findings of the literature, concurs to provide some insights in two open questions concerning the blue vanadium-bearing zircon pigment:

- ✓ the origin of the colour of the pigment, with reference to the conditions of industrial synthesis.
- ✓ the localisation of the V^{4+} site among those available in the structure: dodecahedral (for Zr), tetrahedral (for Si), distorted tetracoordinated (interstitial).

Concerning the first question, our data point out that vivid blue colour are obtained, in line with previous studies [10,41,45], for samples where EPR spectroscopy reveals the unstructured line attributed to V^{4+} clusters. In our opinion, while significantly changing the colorimetric coordinates, the differences in the VIS spectra between the so-called green and blue samples are not so substantial to infer the presence of two active colour systems (e.g. V distributed over two or more different structural sites, and/or mineralogical hosts). Conversely, the presence of V in a single site – occurring either as isolated ions (in diluted samples) or as concentrated ions/clusters (in more concentrated samples, obtained either using the flux technique or the solid-state industrial synthesis) – is likely to explain the whole spectral variability in the VIS region [10,34,41,45,47].

About the second question, our structural and spectroscopic data point to the attribution of the V^{4+} to the interstitial 16*g* site (local symmetry C_2). In this configuration, the only symmetry operator of the $I4_1/amd$ space group acting on the ion is aligned along [110]. The decrease of the symmetry from an ideal tetrahedron, T_d, to a D_{2d} tetragonal bisphenoid, to a C_2 distorted tetracoordinated site implies that all the *d* orbitals of the vanadium ion belong only to two symmetry representations (A and B, see previous chapter). Assuming the reference frame of the V^{4+} orbitals having the C_2 axis as *z* axis, Niesert et al. [45] pointed out by calculations the d_{z2} orbital as the ground state

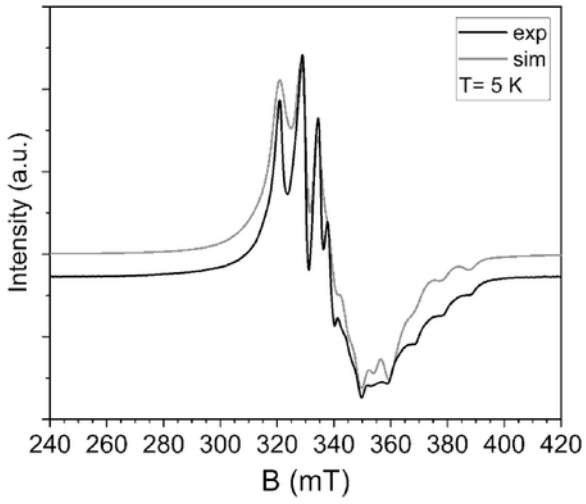

Fig. 9. Detail of the main signal of the experimental X-band ($\nu = 9.402$ GHz) EPR spectrum of the **423** sample (black line), recorded at 5 K and best simulation (grey line) obtained as described in the text.

Table 6
Best fit parameters of the numerical simulation of the EPR spectrum of Fig. 9.

Component	g value	A (cm^{-1})	ΔB (mT)
parallel	1.894 ± 0.001	84 ± 1 × 10^{-4}	3.2 ± 0.2
perpendicular	1.963 ± 0.003	37 ± 3 × 10^{-4}	3.2 ± 0.2

(hosting the single unpaired electron). However, this is fully in contrast with the EPR evidences, according to which a d_x2-$_y2$ should be preferred [10,34,45]. We then performed some qualitative calculations using the Angular Overlap Model (AOM), neglecting e_δ interactions and choosing e_σ and e_π values, providing reasonable orbital energies when compared to observed UV–vis transitions. The results, reported in Table 8, indicate that the ground state, the first excited state and the third one are linear combinations of d_{z2}, d_{xy} and d_x2-$_y$2. By an appropriate choice of the *xy* reference system (which depend on the actual values of e_σ and e_π), the second and fourth excited state are pure d_{xz} and d_{yz}, while the third maintains a dominant d_{xy} character.

A diagram of energy levels of V^{4+} can be drawn, according to the EPR evidences and the results of the calculations, for a decreasing point symmetry (Fig. 10A). The V^{4+} crystal field strength is referred to the energy splitting between the barycentre of the energies of the states originating from the ^2E in T_d symmetry (both ^2A in C_2 symmetry) and those of $^2T_2$ in T_d symmetry on the other side (one ^2A and two ^2B in C_2 symmetry). Since the transition to the first excited state occurs at an energy too low to be observed, the 10*Dq* value was calculated by assuming a constant 1400 cm^{-1} energy for it and averaging those resulting from tetrahedral $^2T_2$ levels (Fig. 10A). For zircon pigments, this procedure provides a value of it is on average 10,920 ± 20 cm^{-1}, slightly lower than the value calculated for the spectrum reported by Di Gregorio et al. [34] that is referred to a zircon with a lower vanadium doping with respect to the industrial pigments in hand.

The strong interplay, and therefore a further indication of converging results, of discussed data is highlighted in Fig. 10B, where the variation of the crystal field strength (10*Dq*) of several V-doped $ZrSiO_4$ samples is contrasted with the amount of tetravalent vanadium in the zircon lattice. According to crystal field theory [59], 10*Dq* values as achieved from EAS can be related to metal-oxygen distances from XRPD by a relationship that in the point charge approximation is close to the inverse fifth power of the mean distances. In the case of the V-doped zircon:

$$10Dq = \text{const}\cdot\langle \text{V—O}\rangle^{-5}, \quad (1)$$

where the constant comprises both the effective charge on the ligand, Q, and the average radius of the *d* orbital, <r>, which are constant for a given metal ion in a given ligand environment [53,59].

Fig. 10B reveals that the crystal field strength of industrial pigments is remarkably lower with respect to that inferred for V-doped zircon samples from the literature [34,42,45]. This circumstance can be readily explained by the different vanadium content, which is significantly higher in the industrial pigments, being 0.07–0.09 apfu (corresponding to one V^{4+} ion every 2.8–3.6 unit cells) versus 0.01–0.03 apfu of samples investigated in the literature (Fig. 10). As pointed out in the paragraph 3.2.2, a larger amount of V^{4+} incorporated at the interstitial 16*g*

Table 7
EPR parameters (g and A principal values, the latter expressed as 10^{-4} cm^{-1}), orbital ground state (GS), colour, site attribution (tet = tetrahedral; dod = dodecahedral) and temperature of measurement (T) as reported in the literature for the V^{4+} in zircon.

Ref.	label	g||	g⊥	A||	A⊥	GS	Colour	Attribution	*T* (K)
[10]	B	1.8930	1.9699	82	29	x^2–y^2	Blue	D_{2d} (tet)	20
[10]	A	1.8930	1.9699	81.6	28.9	xy	Blue	D_{2d} (tet)	20
[34]	A	1.8930	1.9699	82	29	x^2–y^2	Green	D_{2d} (tet)	20
[41]	A	1.8930	1.9699	82	29	–	Blue	D_{2d} (tet + dod)	20
[41]	B	1.8930	1.9699	82	29	–	Blue	D_{2d} (tet + dod)	20
[45]	–	–	–	–	–	x^2	Blue	C_2	*RT*
[47]	C	–	–	–	–	–	Green	D_{2d} (tet + dod)	*RT*
[47]	D	–	–	–	–	–	Green	D_{2d} (tet + dod)	*RT*
[47]	E	1.923	1.975	205	62	–	Blue	C_2	*RT*

Table 8
Energies and orbital composition obtained by AOM calculations, assuming $e_{\sigma 1}$ = 10,000; $e_{\sigma 2}$ = 12,000; $e_{\pi 1}$ = 700; $e_{\pi 2}$ = 800 cm^{-1}. The reference system in the *xy* plane is rotated by 21.85° to have d_{xz} and d_{yz} as pure states.

Energies (cm^{-1})	0	1386	7297	12,937	17,721
Coeff. d_z2	0.7813	0.4935	0	0.3820	0
Coeff. d_{xz}	0	0	1	0	0.
Coeff. d_{yz}	0	0	0	0	1
Coeff. d_{xy}	0.3794	0.1104	0	−0.9186	0
Coeff. d_x2-$_y$2	−0.4955	0.8627	0	−0.1010	0

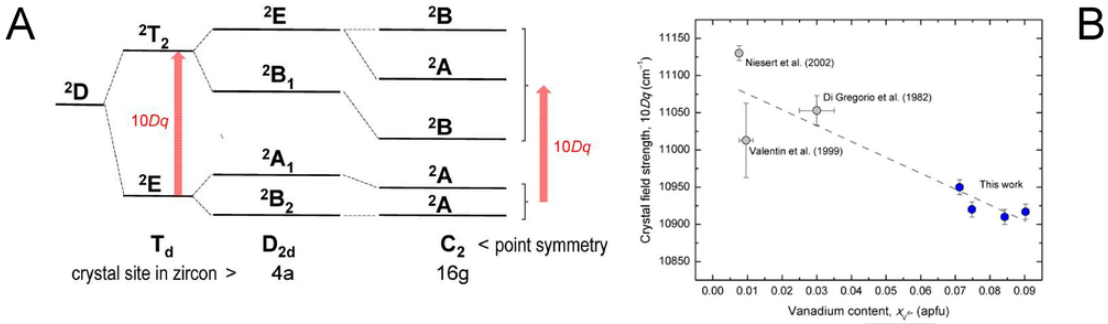

Fig. 10. Energy levels of V^{4+} in tetrahedral coordination with decreasing point symmetry (A). Crystal field strength inferred from electronic absorption spectroscopy as a function of the vanadium content (x_V^{4+}); dashed line is a reader's eye guide (B).

site leads to a longer mean $\langle V^{4+}—O\rangle$ bond distance (Fig. 6C), thus being in qualitative agreement with predictions based on Eq. (1).

Considering that the industrial synthesis is carried out in excess of vanadium, it can be argued that the concentration of V^{4+} measured for the here investigated pigments is likely to be close to the solubility threshold of V^{4+} in the zircon lattice. Indeed, a thorough inspection of the lattice parameters variation suggests that although anisotropic (i.e., the *c*-axis expands more rapidly than *a* with the V^{4+} content, Fig. 5D), the preferential expansion along the chains of edge-sharing SiO_4 and ZrO_8 polyhedra seems to be limited for a V^{4+} content of ~0.06 apfu, i.e. when the *c*-axis reaches ~6.002 Å (Fig. 5C).

Another intriguing aspect in turquoise pigments is that colour saturation (C*) is uncorrelated either to the V content of zircon or to the intensity of the V^{4+} optical bands, but it scales with the pigment particle size (Table 2). As a matter of fact, the turquoise colour of V-doped zircon is due to the window in the optical spectrum allowing the transmission of the wavelengths in the 18,000–25,000 cm^{-1} range (400–550 nm), i.e. the portion of visible light from green to violet (Fig. 11A). The colour perception of human eye is sensitive to the maximum intensity of transmitted light (or conversely to the wavelength of minimum absorbance). Such a minimum absorbance can easily shift from ~20,000 to ~21,000 cm^{-1}, so justifying the frequently observed shades of pigments turning from bluish green to turquoise. Significantly, the colour saturation of industrial pigments is well correlated to the minimum absorbance (Fig. 11B).

The minimum of absorbance is the first derivative (or the tangent point) of the EAS spectrum portion which falls in between the high-energy tail of the ^2A band of V^{4+} – peaking at ~15,600 cm^{-1} with FWHM ~4000 cm^{-1} – and the onset of charge transfer, occurring usually over 22,000 cm^{-1} (Fig. 11A).

The increased intensity of the optical band – once a proper amount of vanadium (> 0.07 apfu) is incorporated in the zircon lattice – can be related to the occurrence of V^{4+}–V^{4+} clusters (previously identified by means of EPR spectra analysis). Such clusters are here intended as a non-homogeneous distribution, where two or more V^{4+} ions occur in the same unit cell and/or in adjacent cells, likely in near 16*g* interstitial sites.

On the other hand, the onset of charge transfer depends on colour centres that absorb the blue to violet (and near UV) wavelengths. The charge transfer absorbance at 25,000 cm^{-1} is minimum for sample **423** and more than double for the others, in the order: **TZ** < **BM61** < **5108** (Fig. 11B). Such colour centres may be induced by mechanical treatment of pigments production, for example the milling process. In principle, more finely ground pigments might suffer of a higher concentration of crystal lattice defects with an ensuing low-energy onset of the charge transfer band. In other words, micronization is simply making more likely – by breaking the zircon crystals into smaller and smaller grains – to have a separation of the adjacent cells bearing V^{4+} ions. Moreover, unconstrained V^{4+} ions occurring at the surface of broken grains lose their colouring power.

Hence, the particle size of pigments could be taken as a crystal lattice defects probe which depends on the intensity of the grinding process. Interestingly, along with the colour saturation, the frequency of the minimum absorbance scales with the median particle size of V-doped zircon (see Table 2). Nonetheless, no direct evidence of such colour centres arose from EPR analyses.

These observations have some relevant repercussions on the pigment synthesis carried out by colorant makers. Overall, an enhanced attention should be paid to both pre-synthesis and post-synthesis operations. About the former stage, the target is to foster the conditions

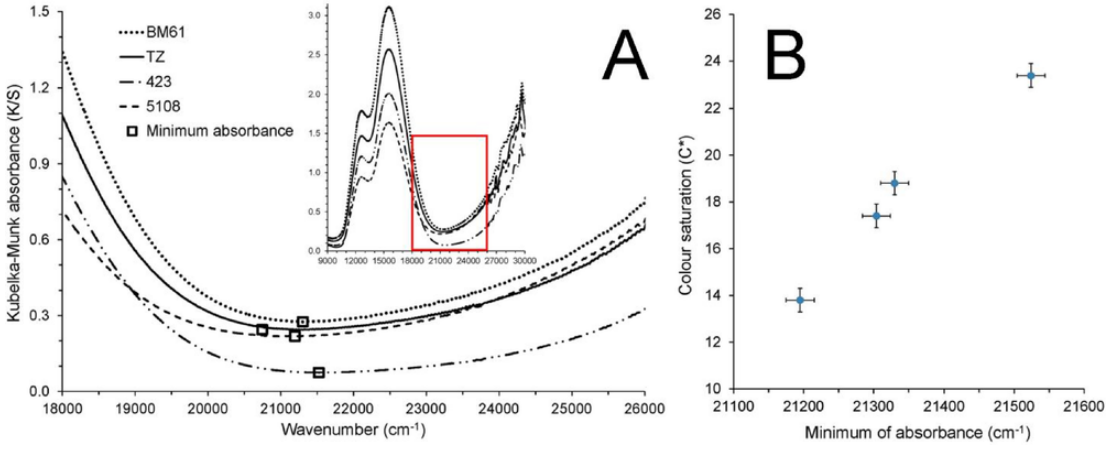

Fig. 11. Portion of the EAS spectra for zircon pigments centred in the visible range with the minimum of absorbance of the transmitted light (A) and the colour saturation C* as a function of the absorbance minimum (B).

leading to the formation of V^{4+} clusters. It implies that V^{4+}–V^{4+} pairs have to be present in the same unit cell of zircon. Thus, a perfectly uniform distribution of the vanadium precursor could be not determinant. A compromise must be found between a satisfactory reaction yield (minimizing the unreacted quartz and baddeleyite that is likely achieved by improving raw materials mixing) and the chance to have a non-homogeneous diffusion of vanadium ions (the kinetics of which probably depends on the conditions of thermal treatment). About the latter stage, it is known that an excessive milling can introduce defects in the zircon structure. These defects may play a double role: to break the V^{4+}–V^{4+} clusters (effect of comminution) and to create undesired colour centres, which could perturb the onset of the charge transfer band in the blue-violet region of visible spectrum. This circumstance could explain why V-doped zircon is so sensitive to micronization [13,14].

5. Conclusions

The literature about the origin of turquoise colour in V-doped zircon outlines a puzzling situation, where aside some well-established points (V^{4+} as chromophore ion in tetrahedral coordination) there are still many unresolved ones. Despite the large number of analytical techniques employed, questions like partition of V^{4+} over different crystal sites, attribution of optical bands, solubility of V in the zircon lattice, or the cause of easy shading from green to blue are still unanswered.

The new EPR and XRPD data here presented converge towards the fact that vanadium is incorporated as V^{4+} at the interstitial site 16*g*, which in zircon has a distorted tetrahedral coordination, with concentrations as high as 0.09 apfu (much higher than the solubility limit previously deemed). Spectroscopic results allow to define the ground state (d_x2-$_y2$) and attribute the main bands in the visible spectrum to the $^2E \leftarrow {}^2T_2$ transition ($^2A \leftarrow {}^2A$ with C_2 point symmetry) whose energy scales with the mean V—O distance, as predicted by the Crystal Field theory. In addition, there are EPR evidences of the occurrence of V^{4+} as both isolated ions and clusters in the industrial pigments. A brighter turquoise colour is observed in the samples with the strongest signal of V^{4+} clusters.

The intensity of turquoise colour in V-doped zircon is related to the window of transmitted light (400–550 nm) and particularly the wavelength of minimum absorbance (~21,000 cm^{-1}) that depends on two optical bands: the tail of the $^2E \leftarrow {}^2T_2$ transition and the onset of charge transfer effects. The former is affected by the occurrence of V^{4+} clusters and the latter by undesired colour centres, likely induced by defects created during pigment comminution. Repercussions on the synthesis procedure of industrial pigments are envisaged and discussed.

Uncited reference

[54].

References

[1] M. Dondi, R.A. Eppler, Ceramic colorants, Ullmann's Encyclopedia of Industrial Chemistry, Wiley-VCH Verlag GmbH & Co. KGaA, Weinheim, 20141–18.

[2] J.B. Vicent, J. Badenes, M. Llusar, M.A. Tena, G. Monrós, Differentiation between the green and Turkish Blue solid solutions of vanadium in a zircon lattice obtained by the sol-gel process, J. Sol-Gel Sci. Technol. 13 (1–3) (1998) 347–352.

[3] G. Costa, M.J. Ribeiro, W. Hajjaji, M.P. Seabra, J.A. Labrincha, M. Dondi, G. Cruciani, Ni-doped hibonite ($CaAl_{12}O_{19}$): a new turquoise blue ceramic pigment, J. Eur. Ceram. Soc. 29 (13) (2009) 2671–2678.

[4] S. Laha, S. Tamilarasan, S. Natarajan, J. Gopalakrishnan, Stabilization of a tetrahedral ($Mn^{5+}O4$) chromophore in ternary barium oxides as a strategy toward development of new turquoise/green-colored pigments, Inorg. Chem. 55 (7) (2016) 3508–3514.

[5] Y. Han, X. Ye, H. Zhu, Y. Li, X. Kuang, New oxygen-deficient cationic-ordered perovskites containing turquoise-coloring $Mn^{5+}O4$ tetrahedral layers, J. Solid State Chem. 247 (2017) 20–23.

[6] C.A. Seabright (1948). Ceramic pigments. U.S. Patent No 2,441,447.

[7] V.I. Matkovich, P.M. Corbett, Formation of zircon from zirconium dioxide and silicon dioxide in the presence of vanadium pentoxide, J. Am. Ceram. Soc. 44 (3) (1961) 128–130.

[8] T. Demiray, D.K. Nath, F.A. Hummel, Zircon-vanadium blue pigment, J. Am. Ceram. Soc. 53 (1) (1970) 1–4.

[9] R.A. Eppler, Mechanism of formation of zircon stains, J. Am. Ceram. Soc. 53 (8) (1970) 457–462.

[10] D. Ball, B.M. Wanklyn, Coloured synthetic zircon crystals, Phys. Status Solidi A 36 (1976) 307–316.

[11] R.A. Eppler, Selecting ceramic pigments, Am. Ceram. Soc. Bull. 66 (11) (1987) 1600–1604.

[12] M. Dondi, M. Blosi, D. Gardini, C. Zanelli, Ceramic pigments for digital decoration inks: an overview, Ceram. Forum Int. 89 (8–9) (2012) E59–E64.

[13] G.L. Güngör, A. Kara, M. Blosi, D. Gardini, G. Guarini, C. Zanelli, M. Dondi, Micronizing ceramic pigments for inkjet printing: part I. Grindability and particle size distribution, Ceram. Int. 41 (5) (2015) 6498–6506.

[14] C. Zanelli, G.L. Güngör, A. Kara, M. Blosi, D. Gardini, G. Guarini, M. Dondi, Micronizing ceramic pigments for inkjet printing: part II. Effect on phase composition and color, Ceram. Int. 41 (5) (2015) 6507–6517.

[15] D. Gardini, M. Blosi, C. Zanelli, M. Dondi, Ceramic ink-jet printing for digital decoration: physical constraints for ink design, J. Nanosci. Nanotechnol. 15 (5) (2015) 3552–3561.

[16] M. Dondi, C. Zanelli, M. Ardit, G. Cruciani, L. Mantovani, M. Tribaudino, G.B. Andreozzi, Ni-free, black ceramic pigments based on Co-Cr-Fe-Mn spinels: a reappraisal of crystal structure, colour and technological behaviour, Ceram. Int. 39 (8) (2013) 9533–9547.

[17] M. Ardit, G. Cruciani, M. Dondi, Structural relaxation in tetrahedrally coordinated Co^{2+} along the gahnite-Co-aluminate spinel solid solution, Am. Mineral. 97 (8–9) (2012) 1394–1401.

[18] G. Cruciani, M. Dondi, M. Ardit, T.S. Lyubenova, J.B. Carda, F. Matteucci, A.L. Costa, Malayaite ceramic pigments: a combined optical spectroscopy and neutron/X-ray diffraction study, Mater. Res. Bull. 44 (8) (2009) 1778–1785.

[19] G. Del Nero, G. Cappelletti, S. Ardizzone, P. Fermo, S. Gilardoni, Yellow Pr-zircon pigments: the role of praseodymium and of the mineralizer, J. Eur. Ceram. Soc. 24 (14) (2004) 3603–3611.

[20] K. Robinson, G.V. Gibbs, P.H. Ribbe, The structure of zircon: a comparison with garnet, Am. Mineral. 56 (1971) 782–790.

[21] R.J. Finch, J.M. Hanchar, Structure and chemistry of zircon and zircon-group minerals, Rev. Mineral. Geochem. 53 (1) (2003) 1–25.

[22] A. Siggel, M. Jansen, Röntgenographische Untersuchungen zur Bestimmung der Einbauposition von Seltenen Erden (Pr, Tb) und Vanadium in Zirkonpigmenten, Z. Anorgan. Allgem. Chem. 583 (1990) 67–77.

[23] K.M. Trappen, R.A. Eppler, Reaction of zirconia with silica at the stoichiometry of zircon, J. Am. Ceram. Soc. 72 (6) (1989) 882–885.

[24] G. Monrós, J. Carda, M.A. Tena, P. Escribano, M. Sales, J. Alarcón, Synthesis and characterization of V_2O_5–SiO_2–ZrO_2 pigments by sol-gel method, J. Non Solids 147 (1992) 588–593.

[25] K.R. Pyon, K.S. Han, B.H. Lee, Formation and colour properties of vanadium doped $ZrSiO_4$ ceramic pigments, J. Ceram. Process. Res. 12 (3) (2011) 279–288.

[26] M. Trojan, Synthesis of a green-blue zirconium silicate pigment, Dyes Pigm. 14 (1) (1990) 9–22.

[27] G. Monrós, J. Carda, M.A. Tena, P. Escribano, M. Sales, J. Alarcón, Different kinds of solid solutions in the V_2O_5–$ZrSiO_4$–NaF system by sol-gel processes and their characterization, J. Eur. Ceram. Soc. 11 (1) (1993) 77–86.

[28] M. Llusar, J.B. Vicent, J. Badenes, M.A. Tena, G. Monros, Environmental optimisation of blue vanadium zircon ceramic pigment, J. Eur. Ceram. Soc. 19 (15) (1999) 2647–2657.

[29] C. Caselli, G. Lusvardi, G. Malavasi, L. Menabue, P. Miselli, Multitechnique approach to V–ZrSiO4 pigment characterization and synthesis optimization, J. Eur. Ceram. Soc. 27 (2) (2007) 1743–1750.

[30] P. Tartaj, C.J. Serna, M. Ocaña, Preparation of blue vanadium-zircon pigments by aerosols hydrolysis, J. Am. Ceram. Soc. 78 (5) (1995) 1147–1152.

[31] J. Alarcón, Crystallization behaviour and microstructural development in $ZrSiO_4$ and V-$ZrSiO_4$ solid solutions from colloidal gels, J. Eur. Ceram. Soc. 20 (11) (2000) 1749–1758.

[32] F.J. Torres, M.A. Tena, J. Alarcón, Rietveld refinement study of vanadium distribution in V^{+4}–$ZrSiO_4$ solid solutions obtained from gels, J. Eur. Ceram. Soc. 22 (12) (2002) 1991–1994.

[33] L.M. Schabbach, F. Bondioli, A.M. Ferrari, T. Manfredini, C.O. Petter, M.C. Fredel, Influence of firing temperature on the color developed by a (Zr,V)SiO_4 pigmented opaque ceramic glaze, J. Eur. Ceram. Soc. 27 (1) (2007) 179–184.

[34] S. Di Gregorio, M. Greenblatt, J.H. Pifer, M.D. Sturge, An ESR and optical study of V^{4+} in zircon-type crystals, J. Chem. Phys. 76 (6) (1982) 2931–2937.

[35] G. Monrós, J. Carda, P. Escribano, J. Alarcón, Synthesis of V-$ZrSiO_4$ solid solutions, J. Mater. Sci. Lett. 9 (2) (1990) 184–186.

[36] P. Chandley, R.J.H. Clark, R.J. Angel, D.G. Price, Site preference of vanadium doped into $ZrSiO_4$ and $ZrGeO_4$ and of terbium doped into $ZrGeO_4$, J. Chem. Soc. Dalton Trans. (9) (1992) 1579–1584.

[37] J. Andrés, A. Beltrán, J. Carda, G. Monrós, V^{4+} doping into SiO_2, ZrO_2 and $ZrSiO_4$ structures. An ab initio perturbed ion study, Int. J. Quantum Chem. 48 (S27) (1993) 175–186.

[38] A. Beltrán, S. Bohm, A. Flores-Riveros, J.A. Igualada, G. Monros, J. Andres, V. Luana, A.M. Pendás, Ab initio cluster-in-the-lattice description of vanadium-doped

zircon: analysis of the impurity centers in vanadium (4+)-doped zircon ($ZrSiO_4$), J. Phys. Chem. 97 (11) (1993) 2555–2559.
[39] A. Beltrán, A. Flores-Riveros, J. Andrés, V. Luana, A. Martín-Pendás, Local relaxation effects in the crystal structure of vanadium-doped zircon. An ab initio perturbed ion calculation, J. Phys. Chem. 98 (32) (1994) 7741–7744.
[40] D.D. de Waal, A.M. Heyns, G. Pretorius, R.J. Clark, Raman spectroscopic investigations of $ZrSiO_4$: V^{4+}, the blue zircon vanadium pigment, J. Raman Spectrosc. 27 (9) (1996) 657–662.
[41] M. Ocaña, A.R. González-Elipe, V.M. Orera, P. Tartaj, C.J. Serna, Spectroscopic studies on the localization of vanadium (IV) in vanadium-doped zircon pigments, J. Am. Ceram. Soc. 81 (2) (1998) 395–400.
[42] C. Valentín, M.C. Muñoz, J. Alarcón, Synthesis and characterization of vanadium-containing $ZrSiO_4$ solid solutions from gels, J. Sol-Gel Sci. Technol. 15 (3) (1999) 221–230.
[43] L. Rubio-Puzzo, C. Caracoche, M.M. Cervera, P.C. Rivas, A.M. Ferrari, F. Bondioli, Hyperfine characterization of pure and doped zircons, J. Solid State Chem. 150 (1) (2000) 14–18.
[44] F.J. Torres, J.V. Folgado, J. Alarcón, Structural evolution and vanadium distribution in the preparation of V^{4+}-$ZrSiO_4$ solid solutions from gels, J. Am. Ceram. Soc. 85 (4) (2002) 794–799.
[45] A. Niesert, M. Hanrath, A. Siggel, M. Jansen, K. Langer, Theoretical study of the polarized electronic absorption spectra of vanadium-doped zircon, J. Solid State Chem. 169 (1) (2002) 6–12.
[46] N. Dajda, J.M. Dixon, M.E. Smith, N. Carthey, P.T. Bishop, Atomic site preferences and structural evolution in vanadium-doped $ZrSiO_4$ from multinuclear solid-state NMR, Phys. Rev. B 67 (2) (2003), 024201.
[47] S. Ardizzone, G. Cappelletti, P. Fermo, C. Oliva, M. Scavini, F. Scime, Structural and spectroscopic investigations of blue, vanadium-doped $ZrSiO_4$ pigments prepared by a sol-gel route, J. Phys. Chem. B 109 (47) (2005) 22112–22119.
[48] A.C. Larson, R.B. Von Dreele, GSAS, General Structure Analysis System, Los Alamos National Laboratory, Los Alamos, NM, 198886–748.
[49] H. Toby, EXPGUI, a graphical user interface for GSAS, J. Appl. Crystallogr. 34 (2001) 210–213.
[50] B.A. Kolesov, C.A. Geiger, T. Armbruster, The dynamic properties of zircon studied by single-crystal X-ray diffraction and Raman spectroscopy, Eur. J. Mineral. 13 (5) (2001) 939–948.
[51] R.J. Hill, L.M.D. Cranswick, IUCr, commission on powder diffraction. Rietveld refinement round robin. II. Analysis of monoclinic ZrO_2, J. Appl. Crystallogr. 27 (1994) 802–844.
[52] W.H. Baur, In search of the crystal structure of low quartz, Z. Kristallogr. 224 (12) (2009) 580–592.
[53] A.S. Marfunin, Physics of Minerals and Inorganic Materials: An Introduction, Springer, Berlin, 1979, p. 340.
[54] Y. Tanabe, S. Sugano, On the absorption spectra of complex ions. I and II, J. Phys. Soc. Jpn. 9 (1954) 753–779.
[55] G. Del Nero, G. Cappelletti, S. Ardizzone, P. Fermo, S. Gilardoni, Yellow Pr-zircon pigments: the role of praseodymium and of the mineralizer, J. Eur. Ceram. Soc. 24 (14) (2004) 3603–3611.
[56] R. Caruba, A. Baumer, M. Ganteaume, P. Iacconi, An experimental study of hydroxyl groups and water in synthetic and natural zircons: a model of the metamict state, Am. Mineral. 70 (11–12) (1985) 1224–1231.
[57] R. Valéro, L. Delmotte, J.L. Paillaud, B. Durand, J.L. Guth, T. Chopin, A new hydrothermal fluoro-zircon, J. Mater. Chem. 9 (1) (1999) 117–123.
[58] R. Shannon, Revised effective ionic radii and systematic studies of interatomic distances in halides and chalcogenides, Acta Crystallogr. A32 (1976) 751–767.
[59] R. Burns, Mineralogical Applications of Crystal Field Theory, 2nd ed., Cambridge University Press, U.K., 1993, p. 576.
[60] A.B.P. Lever, Inorganic Electronic Spectroscopy, 2nd ed., Elsevier, Amsterdam, 1984, p. 863.
[61] G.R. Rossman, Optical spectroscopy, Rev. Mineral. Geochem. 78 (1) (2014) 371–398.
[62] R.L. Frost, Y. Xi, Vibrational spectroscopic study of the minerals cavansite and pentagonite $Ca(V^{4+}O)Si_4O_{10}{\cdot}4H_2O$, Spectrochim. Acta A Mol. Biomol. Spectrosc. 95 (2012) 263–269.
[63] G.R. Rossman, Optical spectroscopy of green vanadium apophyllite from Poona, India, Am. Mineral. 59 (1974) 621–622.
[64] G. Ramakrishnan, M.B.V.L.N. Swamy, P.S. Rao, S. Subramanian, EPR of vanadyl ion in a natural mineral, apophyllite, Proc. Indian Acad. Sci. Chem. Sci. 103 (1991) 613–619.
[65] T.C. Brunold, H.U. Güdel, A.A. Kaminskii, Optical spectroscopy of V^{4+} doped crystals of Mg_2SiO_4 and Ca_2GeO_4, Chem. Phys. Lett. 271 (4–6) (1997) 327–334.
[66] S. Stoll, A. Schweiger, EasySpin, a comprehensive software package for spectral simulation and analysis in EPR, J. Magn. Reson. 178 (1) (2006) 42–55.
[67] G.P. Bernardini, M. Borgheresi, C. Cipriani, F. Di Benedetto, M. Romanelli, Mn distribution in sphalerite: an EPR study, Phys. Chem. Miner. 31 (2004) 80–84.